Multiscalar imaging in partially premixed jet flames with argon dilution

J.H. Frank [a],[*], S.A. Kaiser [a], M.B. Long [b]

[a] *Combustion Research Facility, Sandia National Laboratories, Livermore, CA 94551-0969, USA*
[b] *Department of Mechanical Engineering, Yale University, New Haven, CT 06520-8284, USA*

Abstract

Simultaneous imaging of depolarized and polarized Rayleigh scattering combined with OH-LIF and two-photon CO-LIF provides two-dimensional measurements of mixture fraction, temperature, scalar dissipation rate, and the forward reaction rate of the reaction $CO + OH = CO_2 + H$ in turbulent partially premixed flames. The concept of the three-scalar technique for determining the mixture fraction using CO-LIF with depolarized and polarized Rayleigh signals was previously demonstrated in a partially premixed CH_4/air jet flame [J.H. Frank, S.A. Kaiser, M.B. Long, Proc. Combust. Inst. 29 (2002) 2687–2694]. In the experiments presented here, we consider a similar jet flame with a fuel-stream mixture that is better suited for the diagnostic technique. The contrast between the depolarized and the polarized Rayleigh signals in the fuel and air streams is improved by partially premixing with an argon/oxygen mixture that has the same oxygen content as air. The substitution of argon, which has a zero depolarization ratio, for the nitrogen in air decreases the depolarized Rayleigh signal in the fuel stream and thereby increases the contrast between the depolarized and the polarized Rayleigh signals. We present a collection of instantaneous 2-D measurements and examine conditional means of temperature, scalar dissipation, and reaction rates for two downstream locations. The emphasis is on the determination of the scalar dissipation rate from the mixture-fraction images. The axial and radial contributions to scalar dissipation are measured. The effects of noise on the scalar dissipation measurements are determined in a laminar flame, and a method for subtracting the noise contribution to the scalar dissipation rates is demonstrated.
© 2005 The Combustion Institute. Published by Elsevier Inc. All rights reserved.

Keywords: Turbulent flames; Imaging diagnostics; Mixture fraction; Scalar dissipation; Rayleigh scattering; Laser-induced fluorescence

1. Introduction

Mixture fraction (ξ), scalar dissipation (χ), and reaction rate are fundamental quantities in the study of turbulent combustion but are particularly challenging to measure. Multidimensional measurements of these quantities are needed to improve our understanding of flow–flame interactions in turbulent nonpremixed and partially premixed combustion. The determination of mixture fraction requires simultaneous measurements of all major species and temperature. For multidimensional measurements, it is not fea-

* Corresponding author.
  E-mail address: jhfrank@ca.sandia.gov (J.H. Frank).

sible to measure all of these quantities, so mixture fraction must be determined from a reduced set of measurements. Over the past 23 years, the diagnostic capabilities for measuring mixture fraction in turbulent nonpremixed flames have evolved from single-point Raman/Rayleigh [1–3], UV-Raman [4,5], and Raman/Rayleigh/LIF ([6–9] and references therein) measurements to 1-D [10–16] and 2-D [17–23] techniques. The single-point measurements have provided insights into turbulent nonpremixed flames, and well-documented data sets are currently used for the development of turbulent combustion models via the TNF Workshop [24].

Scalar dissipation, which is defined as $\chi = 2D(\nabla \xi \cdot \nabla \xi)$, where D is the mass diffusivity, requires multidimensional measurements to determine the gradient of mixture fraction. One-dimensional measurements of mixture fraction provide only a single component of the mixture-fraction gradient [10, 16]. To improve on this limitation, the projection of the mixture-fraction gradient onto the flame normal can be determined using simultaneous flame-orientation measurements [11,12]. However, this approach does not provide a direct measurement of the full scalar dissipation rate, and the determination of the flame orientation over a wide range of mixture fractions is challenging. Two-dimensional mixture-fraction imaging affords wide-field measurements of two components of the scalar dissipation and can provide intuitive physical insight into the flame structure. Each image of mixture fraction or scalar dissipation contains on the order of 10^4–10^5 point measurements.

## 1.1. Reduced schemes for determining mixture fraction

Schemes for determining mixture fraction in two dimensions involve the measurement of two or three judiciously selected scalars. Ideally, the measured quantities provide good sensitivity to variations in mixture fraction and have high signal-to-noise ratios. A two-scalar method, which is based on fuel mass fraction (Y_{fuel}) and sensible enthalpy ($h = c_p T$), can be derived by simplifying the chemistry to a one-step reaction between fuel and oxidizer and assuming unity Lewis number [25,26]. In this formulation, the conserved scalar is $\beta = Y_{\text{fuel}} + c_p T/q$, and the mixture fraction is given by

$$\xi_{2\,\text{scalar}} = \frac{\beta - \beta_2}{\beta_1 - \beta_2}$$
$$= \frac{Y_{\text{fuel}} + (c_p T - c_{p,2} T_2)/q}{Y_{\text{fuel},1} + (c_{p,1} T_1 - c_{p,2} T_2)/q}, \qquad (1)$$

where q is the lower heat of combustion per unit mass of fuel, and subscripts 1 and 2 designate the fuel and

oxidizer streams, respectively. This formulation has been used for mixture-fraction imaging in both H_2/air [21] and CH_4/air jet flames [17,18,21]. An iterative procedure is used to determine fuel mass fraction and temperature from measurements of fuel concentration and Rayleigh scattering. In this procedure, laminar flame calculations are used to tabulate the temperature and mixture-fraction-dependent auxiliary variables, which include c_p, the effective Rayleigh cross section, σ_{Ray}, and the mixture molecular weight, W_{mix}. Within the iteration, a "reactedness" can be computed from the local Rayleigh temperature, and the values of c_p, σ_{Ray}, and W_{mix} are linearly interpolated between their values in a laminar flame and in a nonreacting flow [19]. Thus nonequilibrium behavior is taken into account in an approximate fashion for these variables. However, the two-scalar approach has further limitations that stem from the assumption of one-step chemistry. This issue is most prominent in fuel-rich regions where rich-side chemistry converts the parent fuel into intermediate species, which are not accounted for in a one-step reaction. In flames with a significant likelihood of local extinction, one single reaction step is a particularly poor approximation.

These inherent errors in the two-scalar approach can be reduced by measuring an intermediate species and constructing a conserved scalar from three measured quantities. Carbon monoxide is a key intermediate species that can be measured by two-photon LIF. A conserved scalar can be constructed from sensible enthalpy, fuel and CO mass fractions by considering the two-step chemical mechanism for methane oxidation,

$$CH_4 + \tfrac{3}{2}O_2 = CO + 2H_2O + Q_1, \qquad (2)$$

$$CO + \tfrac{1}{2}O_2 = CO_2 + Q_2, \qquad (3)$$
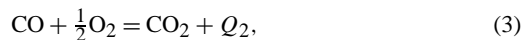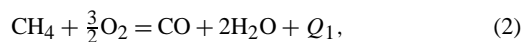
where Q_1 and Q_2 are the heat released per mole of consumed CH_4 and CO, respectively. The expression for a new conserved scalar is derived from the Shvab–Zel'dovich formalism of coupling functions [27]. The simplified unsteady species conservation equation is $L(Y_i) = w_i$, where the operator L is given by $L \equiv \rho \frac{\partial}{\partial t} + \rho \mathbf{v} \cdot \nabla - \nabla \cdot (\rho D \nabla)$, and w_i is the rate of production of species i by chemical reaction. By definition, a conserved scalar has no chemical source term, and therefore $L(\beta) = 0$. The two-step mechanism in Eqs. (2) and (3) can be rewritten on a mass basis as

$$CH_4 + 3O_2 = \tfrac{7}{4}CO + \tfrac{9}{4}H_2O + q_1, \qquad (4)$$

$$CO + \tfrac{4}{7}O_2 = \tfrac{11}{7}CO_2 + q_2, \qquad (5)$$
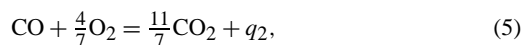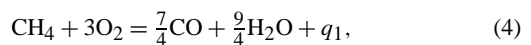
where q_1 and q_2 are the heat released per unit mass of consumed CH_4 and CO, respectively. To derive a conserved scalar, we set $\beta = Y_{\text{fuel}} + a Y_{\text{CO}} + b c_p T$,

apply $L(\beta) = 0$ using Eqs. (4) and (5), and solve for the coefficients a and b. From Eqs. (4) and (5),

$$L(\beta) = w_1(-1 + 7/4a + bq_1) + w_2(-a + bq_2)$$
$$= 0, \tag{6}$$

where w_1 and w_2 are the rates for the first (4) and second (5) reaction steps, respectively. If the two terms in parentheses are set equal to zero, then the coefficients a and b are independent of the reaction rates for the two reaction steps. The resulting coefficients are $a = q_2/q$ and $b = 1/q$, and the conserved scalar is $\beta = Y_{fuel} + q_2/qY_{CO} + c_pT/q$. The three-scalar mixture fraction is given by

$$\xi_{3\,scalar} = \frac{\beta - \beta_2}{\beta_1 - \beta_2}$$
$$= \frac{Y_{fuel} + q_2/qY_{CO} + (c_pT - c_{p,2}T_2)/q}{Y_{fuel,1} + (c_{p,1}T_1 - c_{p,2}T_2)/q}, \tag{7}$$

where $q_2/q = 0.20$ according to the heat-release rates for the two-step mechanism. The mixture fraction, temperature, fuel, and CO mass fractions are determined by an iterative routine that uses the Rayleigh and the CO-LIF signals. Conversion of the CO-LIF signal to CO mass fraction requires an estimate of the variations in Boltzmann fraction and quenching rates. The variations in Boltzmann fraction are determined from the temperature measurements, and the quenching rates are estimated from laminar flame calculations. In the present experiments, we found that using $q_2/q = 0.27$ in the iterative algorithm for determining mixture fraction produced results that were most consistent with detailed point measurements of turbulent jet flames [6,24]. In the remainder of this paper, we will refer to the measured mixture fraction simply as ξ with the subscript "3 scalar" implied.

1.2. Considerations for mixture-fraction imaging

The fuel concentration is central to the reduced formulations of mixture fraction and has previously been measured by LIF of fuel tracers [17], Raman scattering from the fuel [17–19,22], and difference Rayleigh scattering [23,28]. Difference Rayleigh scattering provides the most promising method for imaging the fuel concentration since fuel Raman signals are comparatively weak, and LIF from fuel tracers is plagued by pyrolysis of the tracer [17]. In difference Rayleigh scattering, the polarized and depolarized components of Rayleigh scattering from a polarized laser beam are simultaneously recorded on separate detectors. Rayleigh scattering from isotropic molecules, such as CH_4, contains no measurable depolarized component. In contrast, Rayleigh scattering from anisotropic molecules, such as N_2, O_2, CO_2,

H_2O, H_2, and CO, contains both depolarized and polarized components. The methane concentration can be related to the difference between the polarized and depolarized Rayleigh signals when these signals are normalized to their respective values in air. To ensure that the difference signal is not multivalued with respect to the methane concentration, a linear, or nonlinear, combination of the polarized and depolarized signals can be used instead of the simple difference [23,28].

Fuel mixtures that have no depolarized component provide optimal contrast between the difference Rayleigh signal in the fuel mixture and the air coflow. The use of anisotropic diluent gases, such as nitrogen and oxygen, in the fuel mixture decreases the dynamic range of the difference Rayleigh signal. Partial premixing of methane with air, however, produces more robust flames and significantly reduces broadband fluorescence interference from polycyclic aromatic hydrocarbons. For partially premixed flames, the dynamic range of the difference Rayleigh signal can be significantly improved by replacing the nitrogen in air with a noble gas, which has zero depolarization ratio. In the present study, we consider a fuel mixture that is similar to the Sandia piloted methane/air jet flames A–F in the Turbulent Nonpremixed Flame Workshop (TNF) [6,24] but has argon instead of nitrogen as the inert part of the diluent. The new fuel mixture has the same methane/diluent ratio (1/3 by volume) as the original series of jet flames, but the dilution air is replaced by a mixture of argon and oxygen with the same oxygen content as air. Flames with this new fuel mixture are designated "4Ar" flames to reflect the argon/oxygen ratio (3.76/1 by volume). Piloted jet flames with this fuel composition were previously used for combined Rayleigh/CH_4-Raman/N_2-Raman imaging by Fielding et al. [22]. The argon-diluted flames have a stoichiometric mixture fraction, ξ_{st}, of 0.41, and the air-diluted flames have $\xi_{st} = 0.35$. To match the air-dilution value of ξ_{st} with an argon–oxygen mixture would require an argon/oxygen ratio of 13/1. However, highly turbulent flames with this diluent could not be stabilized on the piloted jet burner.

The increase in air–fuel contrast that is provided by argon dilution is demonstrated in Fig. 1 using calculated Rayleigh signals. The Rayleigh signals in Figs. 1a and 1b were computed from counterflow–flame calculations with air-diluted and argon/oxygen-diluted fuel mixtures, respectively [29,30]. The mixture fraction in these plots was determined from a linear combination of the hydrogen and carbon mass fractions [6]. The oxidizer stream contained room-temperature air, and the global strain rate was $200\ s^{-1}$. The depolarization ratios for computing the depolarized Rayleigh signals are from Fielding
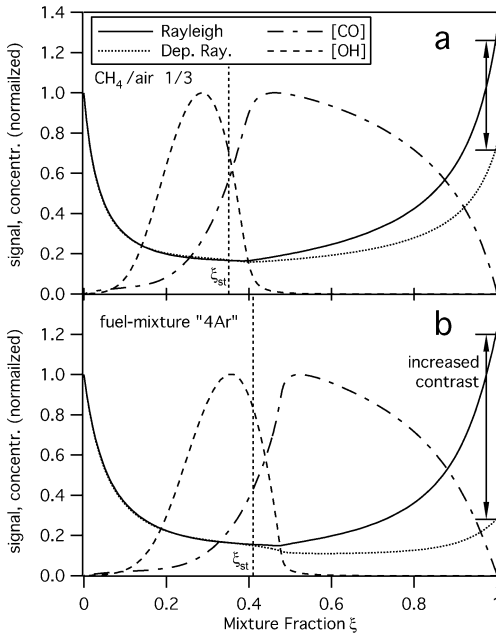
Fig. 1. Predicted polarized and depolarized Rayleigh signals are shown with CO and OH concentrations in air-diluted (a) and argon/oxygen-diluted (b) methane flames with a strain rate of 200 s^{-1}.
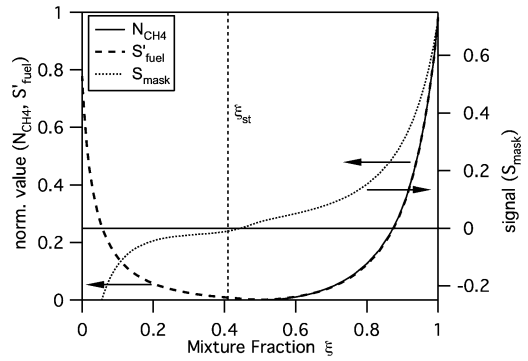

Fig. 2. Comparison of predicted fuel concentration, N_{CH_4}, and surrogate fuel concentration, S'_{fuel}, derived from the polarized Rayleigh signal in an argon/oxygen-diluted methane flame. The mask signal, S_{mask}, eliminates the ambiguity of the multivalued Rayleigh signal.

et al. [28]. Fig. 1 includes plots of the CO and OH concentrations that are normalized with respect to their peak values. A previous study demonstrated that difference Rayleigh scattering can provide a measurement of fuel concentration in an air-diluted methane jet flame, and the result was used for determining the mixture fraction via a three-scalar approach [23]. In the present analysis, emphasis was placed on optimizing the signal-to-noise ratio of 2-D mixture-fraction measurements in flames with a relatively low probability of local extinction. Consequently, the fuel concentration was derived from the polarized Rayleigh signal, which had the largest signal-to-noise ratio of all the measured scalars. A surrogate signal, S'_{fuel}, for the fuel concentration was constructed by subtracting an offset from the polarized Rayleigh signal and normalizing with respect to the signal in the fuel stream ($S'_{fuel} = (S_{Pol} - S_{Polmin})/(S_{Pol,fuel} - S_{Polmin})$, where S_{Polmin} is the minimum polarized Rayleigh signal). Fig. 2 shows a laminar flame calculation of the methane concentration and the predicted fuel surrogate signal normalized to their respective values in the fuel stream. This calculation has a global strain rate of 200 s^{-1}. The variations in S_{Polmin} for strain rates between 100 and 600 s^{-1} are within the noise of the measured Rayleigh signal. On the rich side of ξ_{st}, the curves for S'_{fuel} and the normalized methane concentration show excellent overlap. The polarized Rayleigh signal, however,

is multivalued with respect to mixture fraction, and an additional measurement is needed to eliminate the ambiguity between the rich and the lean regions of the flame. A linear or nonlinear combination of the polarized and depolarized Rayleigh signals can be used to identify the rich and lean regions. This identification is significantly enhanced by the increased contrast between the depolarized and the polarized Rayleigh signals that is afforded by the presence of argon in the diluent. We used the linear combination $S_{mask} = S_{Pol} - 2S_{Dep} + 0.077$ to determine a mask signal, S_{mask}, which was negative for lean conditions and positive for rich conditions. This particular linear combination did not scale with the fuel concentration but instead was chosen to provide a larger slope near stoichiometric conditions to improve the sensitivity of the mask. A binary mask was created by thresholding S_{mask} at 0, and S'_{fuel} was multiplied by the mask to eliminate the ambiguity. The increased contrast provided greater certainty about the local presence or absence of fuel. Alternative schemes for exploiting this increased contrast to determine fuel concentration and mixture fraction in flames with arbitrary degrees of local extinction are under development. These approaches involve a more integrated use of all the measured scalars but may result in larger noise contributions to the measured scalar dissipation rates. In the present analysis, the surrogate for fuel concentration becomes less accurate in regions of localized extinction.

The experimental methods are described below followed by a presentation of results using the three-scalar technique for determining mixture fraction in argon/oxygen-diluted laminar and turbulent jet flames. Mixture-fraction images are used to determine the axial and radial components of the scalar dissipation rate in a turbulent partially premixed methane

jet flame. Images of mixture fraction, scalar dissipation, temperature, and the forward reaction rate for the reaction $CO + OH = CO_2 + H$ are presented. The reaction rate is determined from the OH-LIF and two-photon CO-LIF signals, whose excitation–detection scheme is chosen such that the pixel-by-pixel product is proportional to the forward rate of the reaction $CO + OH = CO_2 + H$ over the relevant range of mixture fractions [23,31]. We estimate the noise contribution to scalar dissipation measurements in a laminar flame and use these results to provide a first-order noise correction for scalar dissipation measurements in a turbulent flame. Conditional means of reaction rate and temperature are presented as a function of scalar dissipation rate.

2. Experimental methods

2.1. Laser and detector arrangement

The experiments were performed in the Advanced Imaging Laboratory at Sandia National Laboratories. Single-shot images of polarized and depolarized Rayleigh scattering, two-photon CO-LIF, and single-photon OH-LIF were simultaneously collected. The experimental facility was similar to that used by Frank et al. [23] and Fielding et al. [28], and is shown schematically in Fig. 3. The beams from five lasers at three wavelengths were combined and focused into a sheet by a fused-silica cylindrical lens (f.l. = 500 mm). Sequential timing of the lasers and detectors eliminated the possibility of crosstalk between the diagnostics. For the Rayleigh measurements, the outputs of two frequency-doubled Nd:YAG lasers at 532 nm were combined by stacking the beams on top of each other at a location 15 m away from the test section. The beams propagated at slightly different angles with respect to the horizontal and merged into a single sheet in the test section. Typical combined energies were approximately 1.7 J/shot. Two-photon CO-LIF was excited by pumping overlapped transitions in the B–X(0, 0) bandhead of the Hopfield–Birge system at 230.1 nm. The frequency-doubled outputs of two Nd:YAG-pumped optical parametric oscillators (OPO) were combined to a typical combined energy of 30–35 mJ/shot at 230.1 nm. The OH-LIF was excited at 285 nm using a frequency-doubled, Nd:YAG-pumped dye laser that was tuned to the Q(12) transition of the A–X(1, 0) band. The 285-nm beam was combined with the 230-nm beams by using a dichroic mirror that reflected 230 nm and partially transmitted 285 nm. The associated energy loss in the 285-nm beam was inconsequential because only a small fraction (0.3 mJ/shot) of the output of the dye laser was used to excite OH-LIF. The overlap of the sheets and each sheet's intensity profile were checked and documented for each experiment by inserting a beam-splitting wedge after the sheet-forming lens and recording the profiles at various distances from the lens. The overall sheet thickness was approximately 200 μm in the center of the imaged region and 250 μm at the edges.

Rayleigh scattering from the probe volume was imaged onto an unintensified interline-transfer camera (640 × 512 pixels after 2 × 2 binning) by a commercial camera lens (f/1.2, f.l. = 50 mm) coupled with a 500-mm achromatic close-up lens. The 600-ns exposure time of the Rayleigh camera suppressed luminous background radiation. On the opposite side of the burner, the depolarized component of the Rayleigh scattering was isolated by a commercial photographic polarizer and a high-throughput interference filter (λ_c = 532 nm, $\Delta\lambda_{FWHM}$ = 10 nm, τ_{max} = 87%) and imaged onto an ICCD camera (512 × 512 pixels, GenIII intensifier) with a camera lens (f/1.2, f.l. = 85 mm) coupled with a 500-mm achromatic close-up lens. The depolarized and polarized Rayleigh images were corrected for shot-to-shot fluctuations in the laser beam profiles. For this purpose, the Nd:YAG beam profiles were recorded for each shot by including a region of ambient air in the polarized Rayleigh image. On the same side as the polarized Rayleigh camera, the OH-LIF signal from the A–X(0, 0) and (1, 1) bands was reflected by a dichroic mirror and imaged onto an ICCD camera (512 × 512, GenII) through suitable color glass filters (UG-11 and WG-295) using a UV-camera lens (Cerco 45 mm, f/1.8) with a 500-mm close-up lens. The average beam profile of the dye laser and the throughput of the imaging optics were measured by recording fluorescence from acetone that was uniformly seeded into an air flow.

The CO fluorescence from the B–A(0, 1) band was detected at 483.5 nm on the same side as the depolarized Rayleigh detection. The CO-LIF signal was separated from the depolarized Rayleigh scattering by a dichroic mirror and was imaged onto an ICCD camera (512 × 512, GenII) by a commercial camera lens (f/1.2, f.l. = 85 mm + 500-mm achromatic close-up lens) with a partially blocked interference filter (λ_c = 484 nm, $\Delta\lambda_{FWHM}$ = 10 nm) to minimize out-of-band interference. Two-photon CO-LIF is particularly sensitive to variations in the laser beam profile because the LIF signal has a nonlinear dependence on laser intensity. The average variations in the OPO laser-sheet intensity were corrected using CO-LIF measurements from a uniform cold flow of dilute CO in N_2 and from the exhaust-gas region of a premixed flat-flame burner. To correct for shot-to-shot fluctuations, Rayleigh scattering from the combined
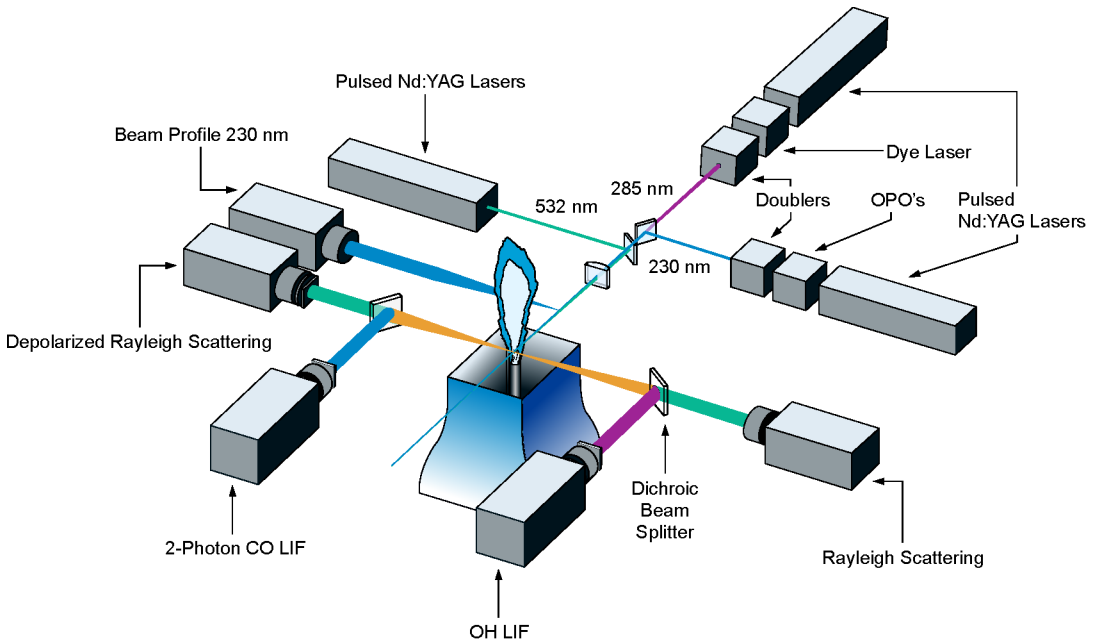
Fig. 3. Experimental configuration for multiscalar imaging measurements. Simultaneous 2-D measurements of depolarized and polarized Rayleigh scattering are combined with OH-LIF and two-photon CO-LIF.

230-nm beams was measured in the air coflow with a fifth ICCD camera (512×512, GenII).

This multiscalar imaging facility was modified from previous studies to improve the measurements. The availability of higher energy lasers for Rayleigh scattering and optimized detection optics improved the signal-to-noise ratio (SNR) of the depolarized Rayleigh signal from 10 to 33 in air. The SNR of the polarized Rayleigh signal in air was 70. The effects of beam steering were significantly reduced by eliminating a retro-reflector and using a single pass of the Rayleigh laser beam. The SNR for the CO-LIF signal was increased from 15 to 23 by improved detection and higher sheet energy. The spatial resolution of the measurements was enhanced by more closely matching the area projected onto each of the detectors. The use of commercial close-up lenses on the Rayleigh, depolarized Rayleigh, and CO-LIF detectors was found to measurably increase the contrast in those images. This enhanced contrast was most evident for the Rayleigh channel, which used an unintensified camera. Finally, the overlapping and characterization of the laser sheets was improved through extensive profiling during alignment.

2.2. Flow conditions

The flow facility, which is identical to that of Refs. [23,28], included a piloted burner that was developed at Sydney University. A set of well-documented point measurements for methane/air jet flames in this burner is available via the TNF Workshop [6,24]. The burner consisted of a 7.2-mm-diameter jet and a 18.2-mm-diameter pilot surrounded by a coflow of filtered air with a mean velocity of 0.9 m/s. For the air-diluted flames, the jet and pilot flows were identical to those in Ref. [6]. For the argon-diluted flames, the lean premixed pilot flame burned a mixture of C_2H_2, H_2, O_2, CO_2, N_2, and Ar having the same equilibrium composition and enthalpy as a premixed mixture of the methane/argon/oxygen fuel mixed with air at an equivalence ratio of 0.68. The argon-diluted flames, Flame A4Ar and D4Ar, had the same flow rates as their air-diluted counterparts, namely the nonpiloted laminar Flame A (Re = 1100) and the turbulent, piloted Flame D (Re = 22,400). Both Flame D and D4Ar have a relatively low probability of extinction. Argon has a lower specific heat than nitrogen, resulting in higher flame temperatures, and the difference in the stoichiometric mixture fraction ($\xi_{st,air} = 0.35$, $\xi_{st,4Ar} = 0.41$) shifts the stoichiometric contour slightly closer to the jet axis. A series of 150 images was acquired for Flames D and D4Ar at axial locations of $x/d = 7.5$ and 15. In the laminar Flames A and A4Ar, 50-shot datasets were recorded at a height above burner of $x/d = 5$.

2.3. Interferences, image registration, and beam steering

To correct the Rayleigh signals for background scattering and crosstalk between the polarized and depolarized signals, images were taken with the field of view flooded by argon, helium, and nitrogen. In the detection of the depolarized Rayleigh signal, a portion of the much stronger polarized Rayleigh component "leaked" into this channel. The corresponding crosstalk factor λ was quantified as described in Fielding et al. [28], and the depolarized images were corrected by subtracting the pixel-by-pixel product of λ and the polarized Rayleigh signal. The camera used for polarized Rayleigh imaging captured a small amount of interference from flame luminosity, due to the limited extinction ratio in the masked region of the interline-transfer CCD chip. It was possible to account for this effect by subtracting an average luminosity image, which was acquired with the gate shifted off the 532-nm laser pulses. Interference from PAH-LIF excited at 532 nm was negligible.

Images from the four scalar channels were registered by imaging a transparent random-dot target, which allowed for checking the mismatch at subpixel resolution using routines from cross-correlation particle image velocimetry (PIV), and then adjusting the registration parameters accordingly. The maximum residual mismatch as determined from the target shots was 2 pixels, occurring in a region near the edge of the images. This region corresponded to pure air in almost all of the shots. The average mismatch toward the center of the images, where the highest scalar gradients are to be expected, was in the subpixel range. Based on the vectors obtained from random-dot PIV, bilinear warping [23] could be employed for further improvement, but this was deemed unnecessary in the current data set. Images from the beam-profiling Rayleigh channel at 230 nm were vertically registered with the CO-LIF images. This was accomplished by inserting an array of thin wires into the beam, creating a suitable intensity pattern in both the 230-nm Rayleigh images and the CO-LIF signal from a uniform flow of nitrogen-diluted CO.

Beam steering due to index-of-refraction gradients is a potential problem for laser measurements in turbulent flames. The effects of such beam steering produced stripes in the Rayleigh images. These stripes could not be corrected using a single beam profile across the entire imaged region because the stripes were inherently not parallel. However, corrections for beam steering were possible with a ray-tracing method, which was based on using the Rayleigh images as an approximate measure of the index-of-refraction field [32]. This ray-tracing technique was applied to the polarized and depolarized Rayleigh images. The effects of beam steering on the scalar statistics presented below were further reduced by only considering data from the side of the flame closest to the lasers and thereby avoiding the region of the worst beam steering. Consequently, the statistical results presented here were not significantly affected by the beam-steering correction. The ray-tracing technique was also used to estimate the effects of beam steering on the scattered light as it traversed the region of the flame between the probe volume and the collection optics. The results indicated that the spread of rays in the image plane was on the subpixel scale and was therefore negligible [32].

3. Results and discussion

3.1. Imaging results from turbulent flames

We first consider a comparison of measurements in the air-diluted and argon/oxygen-diluted turbulent flames. Fig. 4 shows an example of simultaneous single-shot measurements of polarized and depolarized Rayleigh scattering as well as CO-LIF and OH-LIF signals in Flame D. The imaged region is centered 15 diameters downstream of the nozzle exit and spans 4 diameters in the radial direction. The images in the figure have not been smoothed, and the LIF signals have not been corrected for variations in quenching rates or Boltzmann-fraction population. The superior signal-to-noise ratio of the polarized Rayleigh image is apparent. Near the jet centerline, Rayleigh scattering from the low-temperature fuel/air mixture produces a significant signal on the depolarized Rayleigh channel because of the premixing with air. In contrast, images from Flame D4Ar in Fig. 5 show a significantly reduced depolarized Rayleigh signal on the jet centerline due to the substitution of argon for nitrogen. According to the predicted signals in Fig. 1, the difference between the polarized and the depolarized Rayleigh signals in the fuel mixture is a factor of 1.7 greater for the argon/oxygen-diluted fuel mixture than for the air-diluted fuel. This improved contrast significantly enhances the ability to identify the rich and lean regions of the flame.

Fig. 6 shows the mixture-fraction, temperature, and reaction-rate measurements that were determined from the four images in Fig. 5. The mixture-fraction and temperature images were smoothed with a Gaussian smoothing kernel ($\sigma = 0.57$ pixels). This smoothing is advantageous for determining scalar dissipation rates and will be discussed in Section 3.2. The largest mixture-fraction gradients are observed in the fuel-rich region and are indicative of high scalar dissipation rates. The sensitivity of the polarized Rayleigh signal to changes in mixture fraction
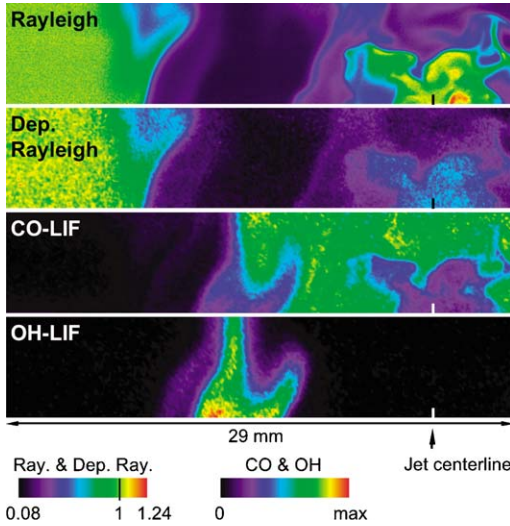
Fig. 4. Sample images of the four measured scalars for Flame D at $x/d = 15$. The Rayleigh signals are normalized by the corresponding values in air. The LIF signals are not corrected for variations in quenching rates or Boltzmann-fraction population.
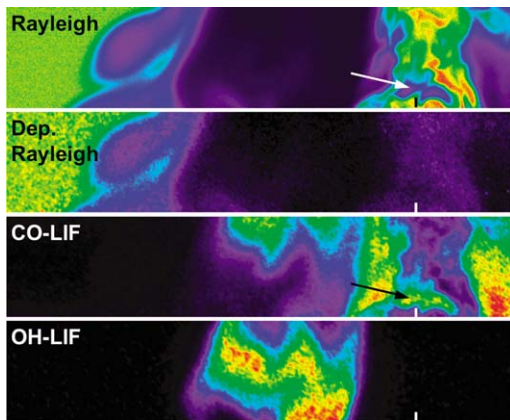

Fig. 5. Sample images for Flame D4Ar at $x/d = 15$. Color scales are the same as in Fig. 4.

is apparent. Near the jet centerline, the polarized Rayleigh image in Fig. 5 shows a pocket with significantly decreased signal where hot gases are entrained into the fuel mixture (indicated by arrow in the figure). The corresponding region in the mixture-fraction image of Fig. 6, however, exhibits a relatively modest decrease in mixture fraction. This sensitivity of the polarized Rayleigh signal is evident from the calculations in Fig. 1b. As the mixture fraction varies from 1.0 to 0.8, the predicted polarized Rayleigh signal decreases by 70%. Similarly, for the lean side, the polarized Rayleigh signal decreases by 78% as the mixture fraction changes from 0 to 0.2. This lean-side sensitivity can be seen by comparing the significant
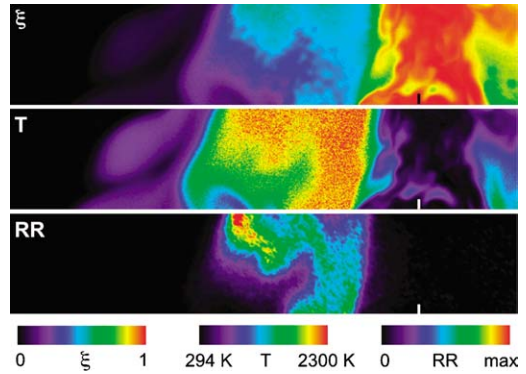

Fig. 6. Single-shot measurements of mixture fraction, temperature, and reaction rate in Flame D4Ar at $x/d = 15$.

change in Rayleigh signal with the modest variation in mixture fraction at the interface between the hot gases and the surrounding air stream on the left-hand side of the images, where large-scale structures entrain air. In the high-temperature regions of the flame, the sensitivity of the Rayleigh signal to mixture fraction decreases. To determine mixture fraction in these regions, it is essential to optimize the signal-to-noise ratio of the Rayleigh measurements, and it is advantageous to have simultaneous CO-LIF measurements.

The CO-LIF signal spans a large portion of the rich region with a packet of CO penetrating into the low-temperature rich region near the jet axis (indicated by arrow in Fig. 5). The reaction-rate image is determined from the pixel-by-pixel product of the CO-LIF and OH-LIF signals without requiring any correction for the variation in the quenching rates and Boltzmann-fraction population. In Fig. 6, the region of appreciable reaction rate spans a relatively broad high-temperature zone and has a width of approximately 3.8 mm at the bottom of the image. In Section 3.3, the reaction-rate images are used to evaluate correlations between reaction rate and scalar dissipation rate.

To appreciate the spatial structures in the turbulent flame, we consider a selection of temperature, scalar dissipation, and reaction-rate images at $x/d = 7.5$ and 15 in Figs. 7 and 8, respectively. The scalar dissipation was determined from the mixture-fraction images by $\chi = 2D((\partial \xi / \partial r)^2 + (\partial \xi / \partial x)^2)$. The images in each figure were selected from the full datasets by sampling every 10th image from the first 100 shots. The images were cropped to a 15.1×5.7-mm subregion and expanded to better show the detailed flame structures. The right side of each image coincides with the jet centerline. Contours of mixture fraction were superimposed onto each of the images in Figs. 7 and 8. The mixture-fraction and temperature images were smoothed with a Gaussian smoothing kernel ($\sigma = 0.57$ pixels) before evaluating the
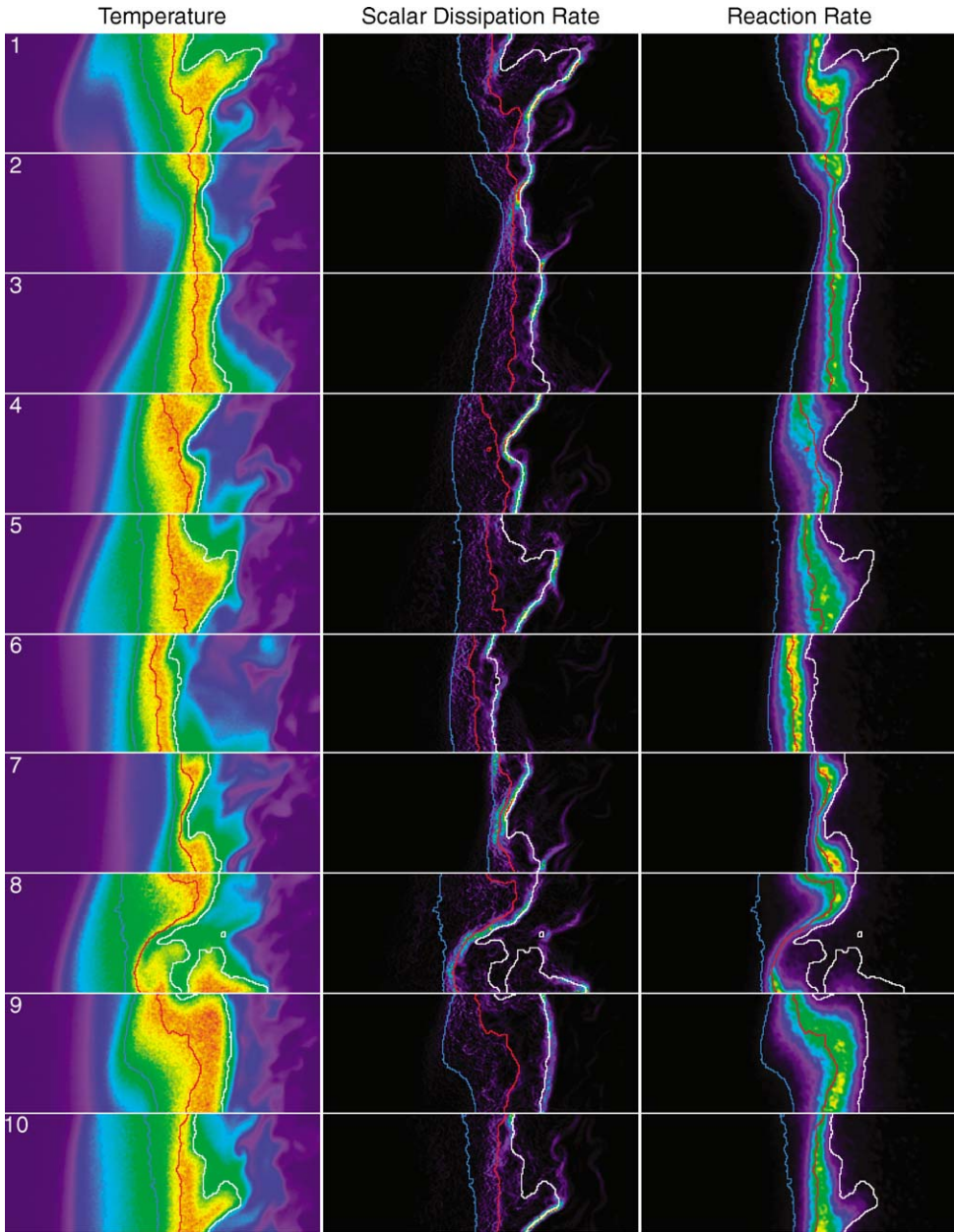
Fig. 7. Single-shot measurements of temperature, scalar dissipation, and reaction rate in Flame D4Ar at $x/d = 7.5$. The superimposed contours of mixture fraction indicate $\xi = 0.21$ (blue), $0.41 = \xi_{st}$ (red), 0.61 (white). Image dimensions are 15.1×5.7 mm, and the jet axis is located at the right edge of each image.

scalar dissipation rate, and the same smoothing was applied to the reaction-rate images. The scalar dissipation rate was determined using fourth-order central differencing to calculate the radial and axial components of the mixture-fraction gradient. The diffusivity, D, was determined from the temperature images using the following fit to the mixture-averaged diffusivity in a counterflow flame calculation with a strain rate of 200 s^{-1}: $D = -0.04992 + 0.4939(T/1000) +$

$1.2539(T/1000)^2$ (cm^2/s). This expression provides a reasonable approximation to the mixture-averaged diffusivity which predominantly depends on temperature. Laminar flame calculations for a range of strain rates indicate that the temperature dependence of the diffusivity is relatively insensitive to the strain rate.

We first consider some general observations from the measurements at $x/d = 7.5$ shown in Fig. 7. The regions of high scalar dissipation rate occur in thin
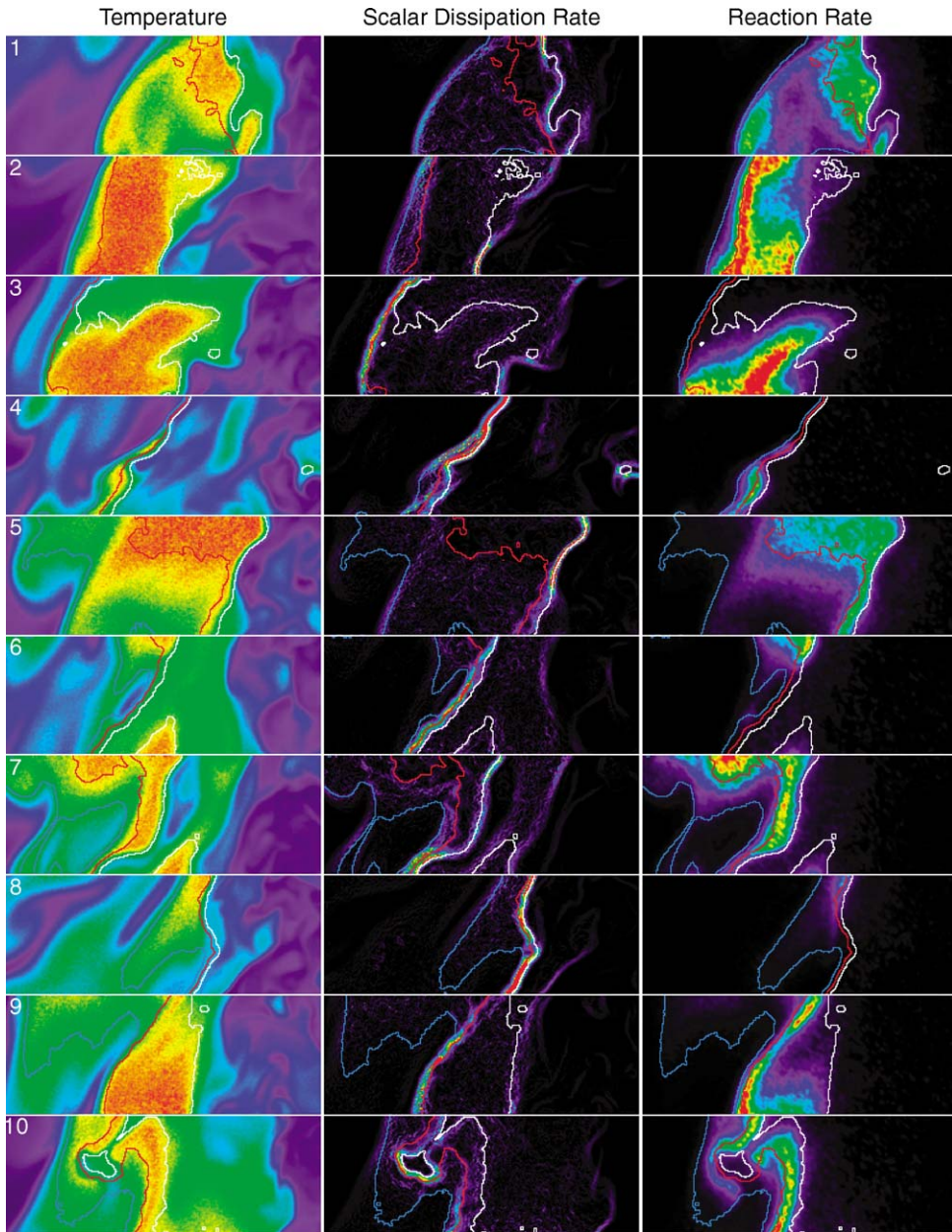
Fig. 8. Single-shot measurements of temperature, scalar dissipation, and reaction rate in Flame D4Ar at $x/d = 15$. The superimposed contours of mixture fraction indicate $\xi = 0.21$ (blue), $0.41 = \xi_{st}$ (red), 0.61 (white). Image dimensions are 15.1×5.7 mm, and the jet axis is located at the right edge of each image.

filaments that are frequently aligned with the rich mixture-fraction contours. The instantaneous reaction zones are relatively closely aligned with the jet axis, and the peak reaction rates occur slightly to the rich side of the stoichiometric contours. In cases where the reaction zone is more convoluted (shots 1, 4, 5, 7, 8, 10), the rich mixture-fraction contour is considerably more distorted than the lean or stoichiometric contours, and in some cases the rich contour extends to-

ward the jet axis well beyond the edge of the reaction zone (shots 1, 4, 5, 8, 10). There is a very low probability of localized extinction at $x/d = 7.5$, as is evident by the continuity of the reaction zones in Fig. 7. However, there are cases where the reaction rate and temperature are locally depressed or the reaction zone is thinner (shots 2, 4, 7, 8). These locations frequently correspond to regions where the rich and stoichiometric mixture-fraction contours are closer together,

and the filaments of high scalar dissipation rate are more likely to overlap with the stoichiometric contour. When there is a local decrease in the temperature near stoichiometric conditions, we expect that the fuel concentration will be overestimated by the surrogate fuel signal. This overestimate will artificially increase the measured mixture fraction at stoichiometric and slightly rich conditions. However, the reaction rate and temperature measurements are expected to remain relatively accurate.

The images in Fig. 8 show that the reaction zones are considerably more convoluted at $x/d = 15$, and the discontinuities in the reaction zones indicate regions of localized extinction. These results are consistent with point measurements that show an increased probability of extinction at the "neck" of the piloted jet flames near $x/d = 15$ for jet flames with a range of Reynolds numbers [6]. The thickness of the reaction zones spans a wider range at $x/d = 15$ than at $x/d = 7.5$. The relatively wide reaction zones observed in several of the reaction-rate images may in part be the result of larger angles between the flame normal and the plane of the laser sheet (shots 1, 2, 3, 5). The filaments of high scalar dissipation are inclined at a steeper angle with respect to the jet axis than at $x/d = 7.5$. The thin and extinguished reaction zones show the same trend as in Fig. 7, such that at these locations the filaments of high scalar dissipation tend to overlap the stoichiometric contour (shots 3, 4, 6, 7, 8, 10). The increased probability of these high-dissipation zones overlapping the stoichiometric contour at $x/d = 15$ is likely to contribute to differences in the conditional mean of scalar dissipation at $x/d = 7.5$ and 15. As will be seen in Section 3.3, the decrease in the rich peak of the scalar dissipation is much more significant than the decrease in the peak near stoichiometric conditions. This difference could in part be explained by an increased occurrence of the overlap between the scalar dissipation filaments and the stoichiometric contour.

Several shots at $x/d = 15$ show a substantial gap between the reaction zone and the lean mixture-fraction contour (shots 5, 7, 8, 9). The images in shot 10 of Fig. 8 are particularly notable since they capture the pinch-off of a fuel-rich pocket as two reaction zones come in close proximity. The lower left face of the pocket is aligned with a filament of high scalar dissipation with the rich and stoichiometric contours close together. This region also exhibits a depressed temperature and reaction rate. These observations represent an initial sampling of the interrelationship between the mixture fraction, scalar dissipation, reaction rate, and temperature fields that result from flow–flame interactions in turbulent jet flames.
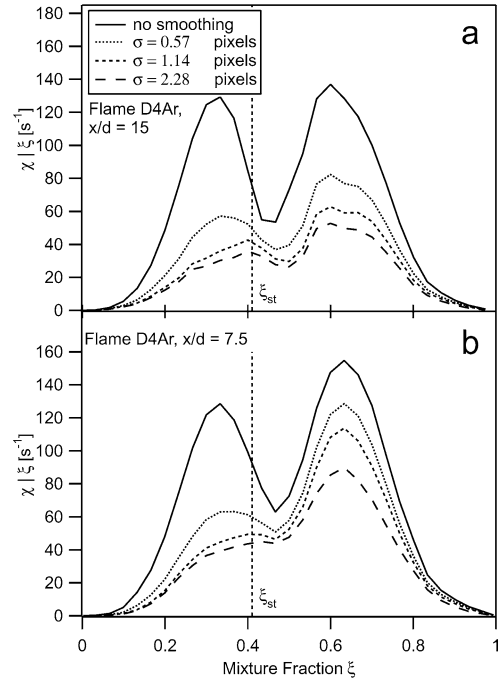

Fig. 9. Conditional scalar dissipation rates in Flame D4Ar at $x/d = 15$ (a) and 7.5 (b) evaluated from mixture-fraction and temperature images that are smoothed by symmetric Gaussian kernels with different widths.

3.2. Noise and resolution

The measurement of scalar dissipation is particularly sensitive to noise in the mixture-fraction images because the scalar dissipation is proportional to the square of the mixture-fraction gradient. Smoothing can reduce the noise at the expense of spatial resolution. We consider the tradeoff between noise reduction and spatial averaging in conditional mean scalar dissipation measurements from 150 shots at two axial locations in Flame D4Ar. The results of smoothing with Gaussian kernels having $\sigma = 0.57$, 1.14, 2.28 pixels are shown in Fig. 9 for $x/d = 7.5$ and 15. The differences in the magnitude and the shape of the scalar dissipation plots result from the combined effects of noise reduction and spatial averaging. As the width of the smoothing kernel is increased, the noise contribution to the scalar dissipation decreases. Spatial averaging is significant when the resolution is too coarse to accurately sample the mixture-fraction gradients. To demonstrate the effects of spatial averaging, we applied the Gaussian smoothing kernels to 1-D laminar counterflow flame calculations [29] with the same $CH_4/O_2/Ar$ fuel-stream mixture as the experiments. While there are limitations to the comparison between laminar flame calculations and turbulent jet flames, it is instructive to consider the effects of
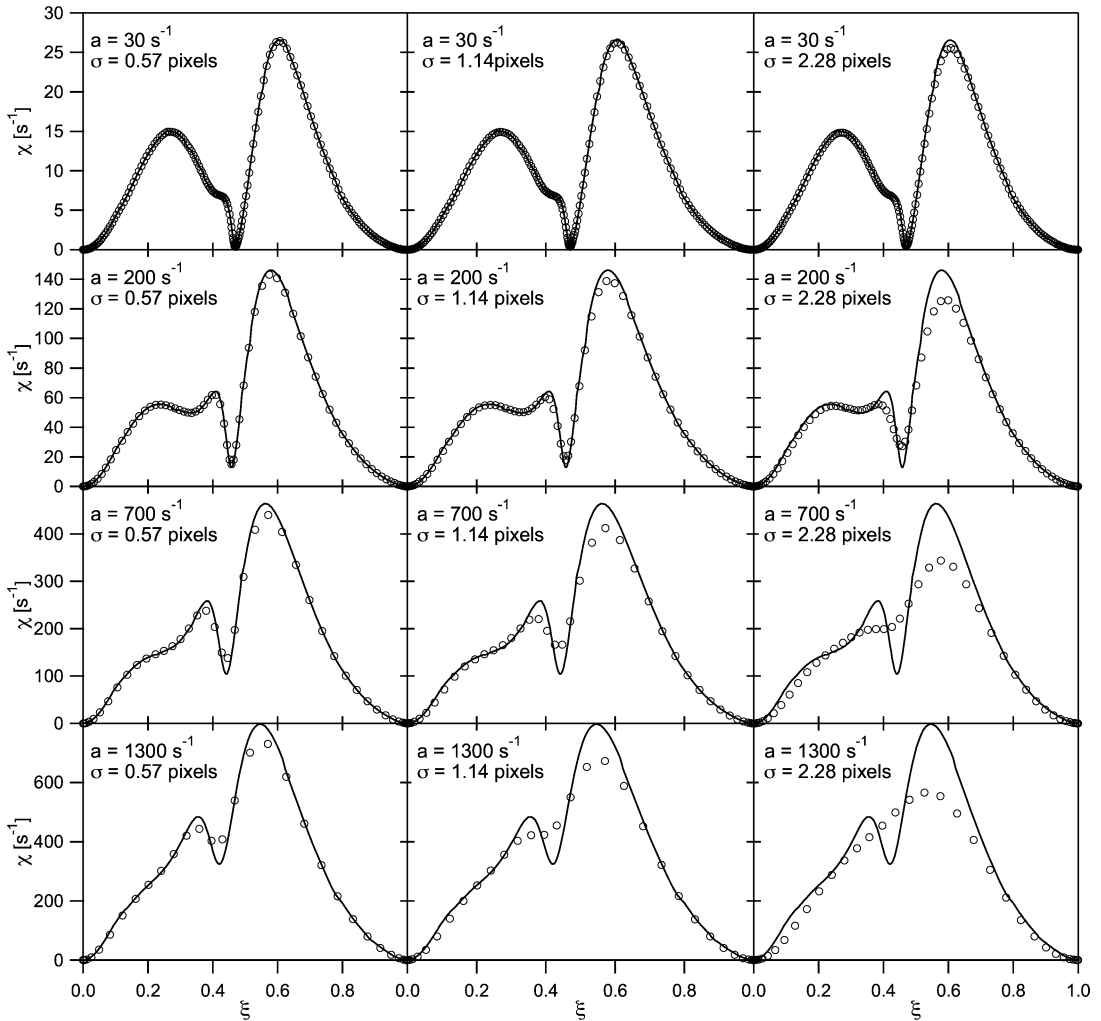
Fig. 10. Laminar flame calculations with the $CH_4/O_2/Ar$ fuel mixture show the effects of spatial averaging on scalar dissipation measurements in flames with strain rates of 30, 200, 700, and 1300 s^{-1}. The spatial averaging is varied by smoothing with Gaussian kernels having $\sigma = 0.57$, 1.14, and 2.28 pixels.

spatial averaging on a laminar flamelet as the strain rate is increased. The original and smoothed results are shown in Fig. 10 for four strain rates ranging from 30 to 1300 s^{-1}. The spacing between the symbols in the plot corresponds to the 58-μm pixel spacing in the experiments. At the two lower strain rates, the spatial scales are well resolved, and smoothing has a negligible impact on the scalar dissipation, with the exception of a minor deviation occurring at a strain rate of 200 s^{-1} and a kernel with $\sigma = 2.28$ pixels. At the two larger strain rates, smoothing with the largest kernel further reduces the peak scalar dissipation and eliminates the trough near stoichiometric conditions. The results for the narrowest kernel ($\sigma = 0.57$ pixels) indicate that smoothing has minor effects even at strain rates of 1300 s^{-1}. The width of this smoothing kernel is comparable to the width of the measured

line spread function for the polarized Rayleigh imaging system.

The noise contribution in the scalar dissipation measurements after Gaussian smoothing with a kernel of $\sigma = 0.57$ pixels can be estimated by considering a laminar flame in which one component of the mixture-fraction gradient is negligible. Fig. 11 shows single-shot Gaussian-smoothed measurements of mixture fraction, temperature, and scalar dissipation rate at $x/d = 5$ in Flame A4Ar. Over the imaged area, the average mixture-fraction gradient in the axial direction is negligible. Consequently, the axial component of the scalar dissipation determined from an average mixture-fraction image, $2D(\partial\langle\xi\rangle/\partial x)^2$, is approximately zero. However, the measured axial component of scalar dissipation in a single-shot measurement is nonzero because it is dominated by
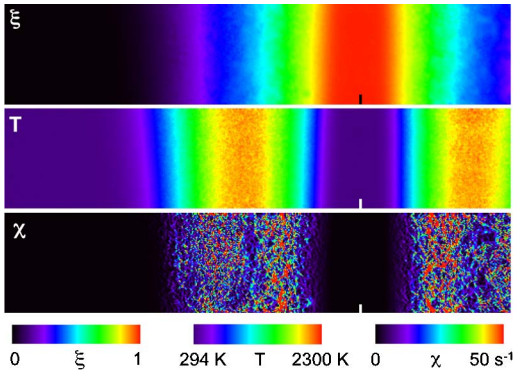
Fig. 11. Single-shot measurements of mixture fraction, temperature, and scalar dissipation from Flame A4Ar at $x/d = 5$.
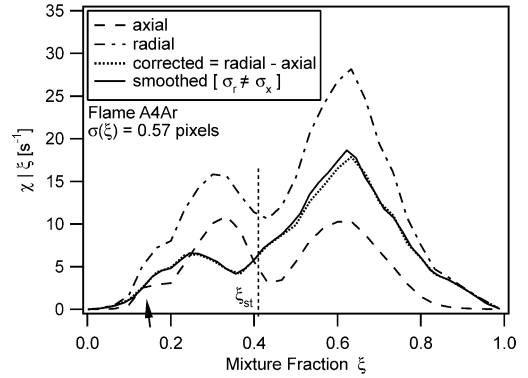

Fig. 12. Conditional means of radial and axial components of scalar dissipation in laminar Flame A4Ar at $x/d = 5$ after smoothing the mixture-fraction and temperature images by a symmetric Gaussian kernel ($\sigma_r = \sigma_x = 0.57$ pixels). The axial component represents the noise contribution. The difference between the radial and axial components (dotted line) is the noise-corrected scalar dissipation. The solid line is the best estimate of the true scalar dissipation based on smoothing with an elliptical Gaussian kernel ($\sigma_r = 1.7$ pixels, $\sigma_x = 10$ pixels).

the noise in the mixture-fraction and temperature images. The conditional mean noise contribution to the scalar dissipation measurements can be determined in the laminar flame by $\langle \chi_x^{\mathrm{noise}} | \xi \rangle = 2D(\partial \xi / \partial x)^2$. Fig. 12 shows the conditionally averaged axial and radial components of the scalar dissipation, which were evaluated from a series of 50 shots in Flame A4Ar. The slight "shoulder" around $\xi = 0.15$ (indicated by the arrow) is attributable to a minor lean-side artifact introduced in the calculation of mixture fraction. The mean radial component of scalar dissipation, $\langle \chi_r^{\mathrm{meas}} | \xi \rangle = 2D(\partial \xi / \partial r)^2$, is the sum of the actual scalar dissipation and the noise contribution, χ_r^{noise}.

In principle, if the conditional mean noise contribution, $\langle \chi_r^{\mathrm{noise}} | \xi \rangle$, is known, then it can be subtracted from $\langle \chi_r^{\mathrm{meas}} | \xi \rangle$ to obtain an improved measurement of the conditional mean scalar dissipation. If the noise statistics are comparable in the axial and radial directions, then $\langle \chi_r^{\mathrm{noise}} | \xi \rangle = \langle \chi_x^{\mathrm{noise}} | \xi \rangle$, and the corrected mean scalar dissipation can be determined by $\langle \chi_r^{\mathrm{corr}} | \xi \rangle = \langle \chi_r^{\mathrm{meas}} | \xi \rangle - \langle \chi_x^{\mathrm{noise}} | \xi \rangle$. This noise-corrected scalar dissipation is shown by the dotted curve in Fig. 12. To verify the validity of this correction in the laminar flame, we compared the noise-corrected scalar dissipation with the scalar dissipation obtained from a mixture-fraction image that was smoothed to the point of having negligible noise, $\langle \chi^{\mathrm{smo}} | \xi \rangle$. This more extensive smoothing was performed using an elliptical Gaussian kernel ($\sigma_r = 1.7$ pixels, $\sigma_x = 10$ pixels), which preserved the radial gradients while significantly reducing the noise. The preservation of the gradients was verified by comparing radial profiles of mixture fraction from the smoothed and unsmoothed images. In Fig. 12, the excellent agreement between $\langle \chi_r^{\mathrm{corr}} | \xi \rangle$ and $\langle \chi^{\mathrm{smo}} | \xi \rangle$ indicates that the noise correction works quite well in Flame A4Ar.

In turbulent flames, we performed a similar correction to the scalar dissipation using the laminar

flame results as a first-order estimate of the noise contribution to the scalar dissipation. The total noise contribution to the scalar dissipation, χ^{noise}, is the sum of the axial and radial contributions, $\chi^{\mathrm{noise}} = \chi_x^{\mathrm{noise}} + \chi_r^{\mathrm{noise}}$. If the noise statistics of scalar dissipation are comparable in the axial and radial directions, then the total noise can be estimated as twice the axial noise contribution, and the noise-corrected scalar dissipation is given by $\chi^{\mathrm{corr}} = \chi^{\mathrm{meas}} - 2\chi_x^{\mathrm{noise}}$, where χ_x^{noise} is determined from Flame A4Ar. This first-order estimate of the noise contribution to the scalar dissipation assumes that χ^{noise} is only dependent on mixture fraction. Higher order corrections that would account for variations in χ^{noise} as a function of χ are currently under investigation.

Fig. 13 shows the measured and noise-corrected conditional scalar dissipation at $x/d = 7.5$ and 15. The slight dip in the noise-corrected dissipation at $\xi = 0.15$, which also will be discernible in some of the subsequent figures, is caused by the artifact that was discussed for Fig. 12. At both downstream locations, the measured scalar dissipation exhibits peaks at lean and rich conditions. The noise correction slightly shifts the lean peak toward the stoichiometric mixture fraction. For the rich peaks, the noise correction is 16 and 24% of the scalar dissipation measured at $x/d = 7.5$ and 15, respectively. From $x/d = 7.5$ to 15, the noise-corrected rich scalar dissipation peak decreases by 43%, and the lean peak decreases by 25%. The magnitude, shape, and axial progression of the scalar dissipation plots agree well with line measurements in Flame D [11]. The line
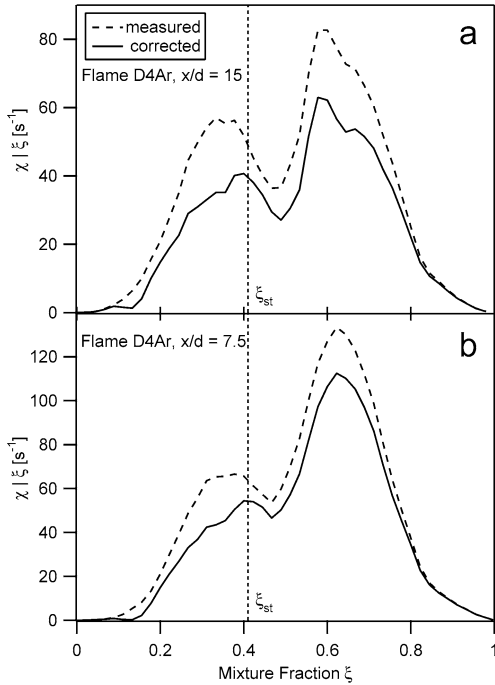
Fig. 13. Measured and noise-corrected conditional mean scalar dissipation rates in Flame D4Ar at $x/d = 15$ (a) and 7.5 (b) with Gaussian smoothing ($\sigma = 0.57$ pixels) of the mixture-fraction images.
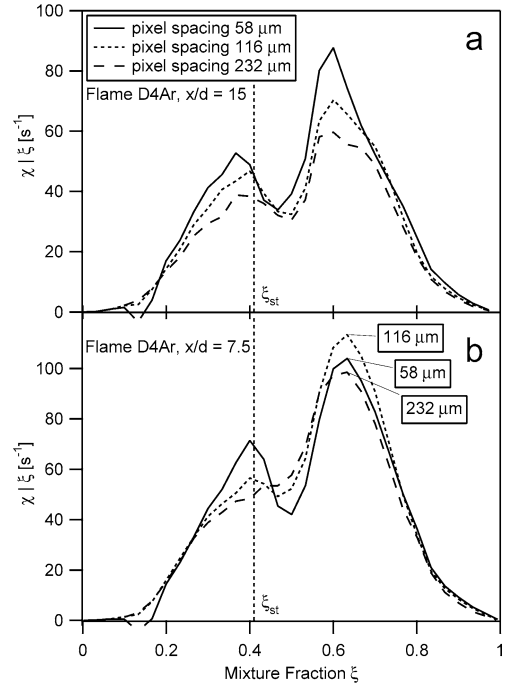
Fig. 14. Noise-corrected conditional mean of scalar dissipation determined from unsmoothed mixture-fraction and temperature images with the pixel spacing increased to 116 and 232 μm by sampling every second and fourth pixel, respectively. Data are from $x/d = 15$ (a) and 7.5 (b).

measurements, however, show a single peak in the scalar dissipation on the rich side and a plateau, or shoulder, near stoichiometric conditions. These differences may result from a combination of factors, including a lower spatial resolution in the line measurements, the substitution of Ar for N_2 in flames considered here, and the different definitions of mixture fraction.

The ability to subtract the noise contribution from the measured scalar dissipation rates makes it possible to isolate the effects of spatial averaging in the turbulent flame data. The spatial resolution was artificially reduced by sampling the unsmoothed mixture-fraction and temperature images with a coarser pixel spacing, and the resulting scalar dissipation rates were corrected for the noise contribution at the respective resolution. Fig. 14 compares the noise-corrected scalar dissipation rates using the native pixel spacing as well as every second and fourth pixel, corresponding to pixel spacings of 58, 116, and 232 μm, respectively. In general, degrading the resolution yields a decrease in the peaks of the scalar dissipation, which is consistent with the results of the laminar flame calculations shown in Fig. 10 and discussed above. The local minimum in the scalar dissipation becomes less prominent as the resolution is degraded. At $x/d = 7.5$ the trough in the scalar dissipation

plot is eliminated at a resolution of 232 μm. However, at $x/d = 7.5$, the dissipation values near the rich peak are lower at the native pixel spacing than they are with 116-μm spacing, indicating the limitations of this noise correction scheme for high levels of noise. For the rich peak in scalar dissipation, the noise correction with the native pixel spacing is $\langle \chi_x^{\text{noise}}|\xi \rangle = 57$ s^{-1}, which is approximately 30% of the uncorrected scalar dissipation. For reduced resolutions, the noise correction decreases as the inverse square of the pixel spacing. A comparison of Figs. 13 and 14 indicates good agreement between the noise-corrected scalar dissipation rates with Gaussian smoothing ($\sigma = 0.57$ pixels) and 116-μm sampling. Further smoothing is likely to eliminate features that contribute to the local minimum in scalar dissipation near $\xi = 0.5$, which is slightly on the rich side of the peak reaction rate for $CO + OH$. These results suggest that Gaussian smoothing with $\sigma = 0.57$ pixels is a reasonable compromise between retaining the best resolution possible and suppressing noise.

In general, the appropriate degree of smoothing will depend on the spatial scales present within the flame and will vary with axial location. The Batchelor scale, λ_B, is commonly used as an estimate for the

resolution requirements. In the self-similar region of jet flows that are dominated by mixing, the Batchelor scale can be evaluated as $\lambda_B = C\delta\,\mathrm{Re}^{-3/4}\,\mathrm{Sc}^{-1/2}$, where Re and Sc are the Reynolds and Schmidt numbers, respectively, and C is an empirical constant that depends on the flow configuration and the definition of the characteristic velocity and length scale, δ. While this expression may be applicable in the far field of a reacting jet where the flow is dominated by mixing, the determination of λ_B is ambiguous in the near field of a jet flame where reactions affect the flow scales. Estimates of λ_B in Flame D at $x/d = 15$ using single-point measurements of the temperature and major species [6] span an order of magnitude when $C = 1$–2 and the temperature that is used for determining the flow properties is varied between the jet centerline value and the maximum in the mean radial profile. This uncertainty indicates that alternative approaches to determining resolution requirements are needed.

A unique aspect of 2-D scalar dissipation measurements is the ability to examine the contribution of two different components of scalar dissipation. The noise-correction technique can be applied separately to the conditional mean of the axial and radial components of scalar dissipation in the turbulent flame. Figs. 15a and 15b compare the axial and radial components of scalar dissipation at two downstream locations. Each component has been corrected for the conditional mean noise contribution by subtracting $\langle\chi_x^{\mathrm{noise}}|\xi\rangle$, which was determined from Flame A4Ar, as previously described. The scalar dissipation is dominated by the radial component. At the rich peak, the radial component is a factor of 4.0 and 2.9 greater than the axial component for $x/d = 7.5$ and 15, respectively. From $x/d = 7.5$ to 15, the radial and axial components of the rich peak decrease by 50 and 33%, respectively. In principle, the imaging data could also be used to determine the projection of the axial and radial components of $\nabla\xi$ onto the flame-normal coordinates, where the local flame normal is specified from the mixture-fraction contours.

3.3. Reaction rate and temperature vs scalar dissipation

Turbulent diffusion flame theory predicts the scaling of reaction rate with scalar dissipation rate, thus relating the reaction rate to the molecular mixing rates [33]. It is therefore of great interest to measure reaction-rate statistics conditioned on scalar dissipation rate and mixture fraction. The results of the imaging measurements can provide such statistics. As an example, the conditional means of temperature and reaction rate as a function of scalar dissipation rate are shown in Figs. 16a and 16b, respectively. The results
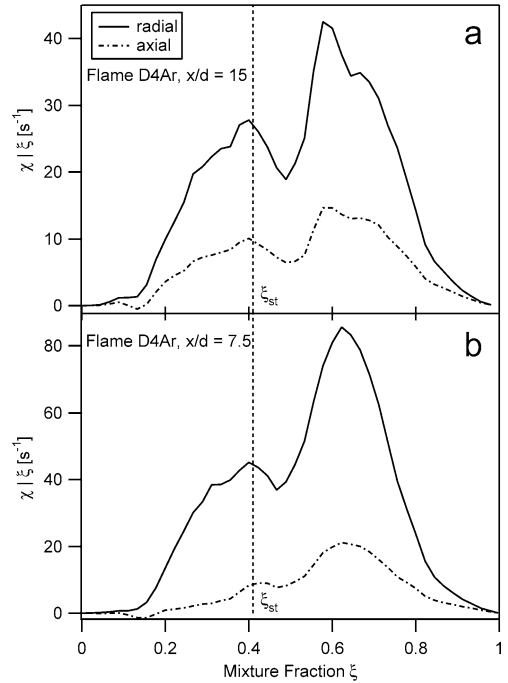

Fig. 15. Noise-corrected conditional mean of axial and radial components of scalar dissipation at $x/d = 15$ (a) and 7.5 (b) with Gaussian smoothing ($\sigma = 0.57$ pixels) of the mixture-fraction images.

are doubly conditioned on scalar dissipation rate and a mixture-fraction interval of $0.4 < \xi < 0.5$, which approximately corresponds to the region of peak reaction rate for the $CO + OH$ reaction. The conditional mean temperature monotonically decreases with increasing scalar dissipation rate. The reaction rate shows a slight increase at low scalar dissipation rates and then decays for $\chi > 100\ \mathrm{s}^{-1}$. At the highest scalar dissipation rates, the depressed temperatures and reaction rates are the result of an increased probability of localized extinction. The images in Figs. 7 and 8, which were described in Section 3.1, show the types of flame structures that contribute to localized decreases in reaction rate and temperature.

Fig. 16 includes results from a set of laminar flame calculations with strain rates ranging from 50 to 1370 s^{-1} in increments of 10 s^{-1}. At each strain rate, the temperature, reaction rate, and scalar dissipation rate were averaged over the mixture-fraction interval of $0.4 < \xi < 0.5$. The reaction rate was computed by $k(T)[OH][CO]$, where the rate constant, $k(T)$, was specified by Gri-Mech 3.0 [30]. The laminar flame calculations indicate trends similar to those of the measurements for both the temperature and the reaction rate. Detailed agreement between the calculations and measurements is not expected since the
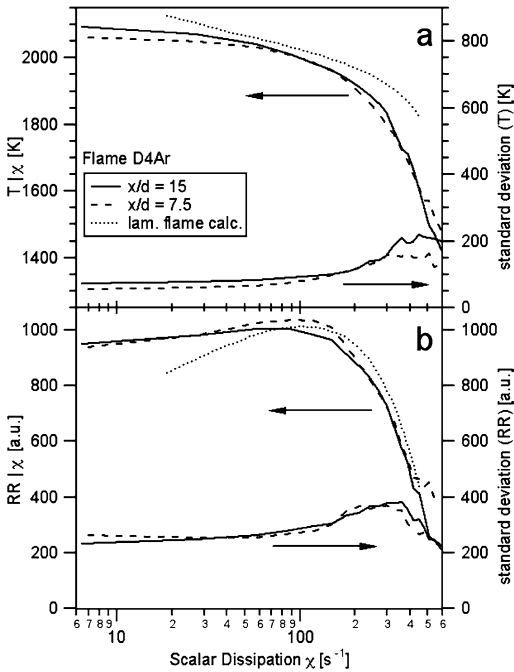
Fig. 16. Conditional mean and standard deviation of temperature (a) and reaction rate (b) at $x/d = 15$ and 7.5. The values are doubly conditioned on scalar dissipation rate and the mixture-fraction interval of 0.4–0.5.

calculations do not capture unsteady effects, such as extinction or ignition.

The reaction $CO + OH = CO_2 + H$ is the primary pathway for CO_2 production in CH_4/air flames, and the reaction-rate results presented here indicate the behavior of only one portion of the full reaction mechanism. In the future, it would be interesting to compare reaction rates from different parts of the reaction mechanism. For example, the addition of formaldehyde LIF coupled with OH-LIF imaging could provide a measure of a reaction rate that may be more closely correlated with the local heat release rates [34,35].

4. Conclusions

Multiscalar imaging of depolarized and polarized Rayleigh scattering combined with OH-LIF and two-photon CO-LIF provided simultaneous measurements of temperature, mixture fraction, scalar dissipation rate, and the forward reaction rate of the reaction $CO + OH = CO_2 + H$. The technique was demonstrated in a partially premixed turbulent jet flame with a CH_4/O_2/Ar fuel-stream mixture. The flame considered here (Flame D4Ar) had the same fuel/diluent ratio (1/3 by vol) and jet velocity as the air-diluted Sandia Flame D investigated by Barlow and Frank [6].

In the modified fuel mixture, the N_2 from air was replaced with Ar to enhance the contrast of the depolarized and polarized Rayleigh signals between the fuel and air streams. The enhanced contrast facilitated the identification of the rich and lean regions of the flame, which improved the mixture-fraction measurements.

The mixture fraction was determined by a three-scalar formulation using the depolarized and polarized Rayleigh signals combined with the CO-LIF signal. The emphasis here was on providing measurements of mixture fraction and its gradient with improved signal-to-noise ratios compared to previous experiments [23]. The radial and axial components of the scalar dissipation were determined from the mixture-fraction images. Analysis of the tradeoff between noise reduction and spatial averaging with image smoothing showed that a Gaussian smoothing kernel ($\sigma = 0.57$ pixels) significantly reduced the noise contribution to the scalar dissipation measurements and that more significant smoothing eliminated details in the conditional mean of scalar dissipation rate at $x/d = 7.5$. The noise contribution to the scalar dissipation measurements was evaluated in a steady laminar flame (Flame A4Ar), and the results were used to perform a first-order correction for the noise contribution in a turbulent flame.

A collection of instantaneous 2-D measurements of mixture fraction, temperature, scalar dissipation rate, and reaction rate was presented. The regions of high scalar dissipation rate were confined to thin filaments. At $x/d = 7.5$, these filaments were primarily aligned with a rich mixture-fraction contour of $\xi = 0.61$, which approximately corresponded to the peak in the conditional mean scalar dissipation rate. Regions with depressed temperatures and reaction rates frequently coincided with filaments of high scalar dissipation overlapping the stoichiometric contour as the rich and stoichiometric contours came in close proximity. These events were more frequent at $x/d = 15$, where extinction events were more probable and the reaction zone was more convoluted. This increased overlap between the scalar dissipation filaments and the stoichiometric contour was likely a factor in the observed differences in conditional means of scalar dissipation rate at $x/d = 7.5$ and 15. Overestimates of the fuel concentration in regions of depressed temperature are expected to introduce localized errors in the mixture fraction, while the reaction rate and temperature measurements are expected to remain relatively accurate.

The imaging results presented here provide an initial glimpse into the spatial relationships of the mixture fraction, scalar dissipation, temperature, and reaction-rate fields. We anticipate that a great deal more will be learned from further studies of the data,

including an analysis of correlations of scalar dissipation rate and reaction rate with flame curvature. The development of the diagnostic technique for application to flames with considerably higher probabilities of localized extinction is ongoing. Comparisons of multiscalar imaging measurements with single-point and 1-D measurements will provide a more complete understanding of flow–flame interactions in turbulent nonpremixed and partially premixed flames. The availability of two-dimensional measurements is expected to help advance modeling efforts and is particularly well suited for comparisons with large-eddy simulations.

Acknowledgments

References

[1] M.C. Drake, S.H. Stårner, R.W. Bilger, Proc. Combust. Inst. 19 (1982) 459–467.

[2] R.W. Dibble, W. Kollman, R.W. Schefer, Combust. Flame 55 (1984) 307–321.

[3] S.H. Stårner, R.W. Bilger, R.W. Dibble, R.S. Barlow, Combust. Sci. Technol. 86 (1992) 223–236.

[4] T.S. Cheng, J.A. Wehrmeyer, R.W. Pitz, Combust. Flame 91 (1992) 323–345.

[5] F. Lipp, J. Hartick, E.P. Hassel, J. Janicka, Proc. Combust. Inst. 24 (1992) 287–294.

[6] R.S. Barlow, J.H. Frank, Proc. Combust. Inst. 27 (1998) 1087–1095.

[7] R.S. Barlow, A.N. Karpetis, J.H. Frank, J.-Y. Chen, Combust. Flame 127 (2001) 2102–2118.

[8] V. Bergmann, W. Meier, D. Wolff, W. Stricker, Appl. Phys. B 66 (1998) 489–502.

[9] W. Meier, R.S. Barlow, Y.L. Chen, J.-Y. Chen, Combust. Flame 123 (2000) 326–343.

[10] A.N. Karpetis, R.S. Barlow, Proc. Combust. Inst. 29 (2002) 1929–1936.

[11] A.N. Karpetis, R.S. Barlow, Proc. Combust. Inst. 30 (2004) 665–672.

[12] A.N. Karpetis, T.B. Settersten, R.W. Schefer, R.S. Barlow, Opt. Lett. 29 (2004) 355–357.

[13] S.P. Nandula, T.M. Brown, R.W. Pitz, Combust. Flame 99 (1994) 775–783.

[14] Y.-C. Chen, M.S. Mansour, Combust. Sci. Technol. 126 (1997) 291–313.

[15] A. Brockhinke, S. Haufe, K. Kohse-Höinghaus, Combust. Flame 121 (2000) 367–377.

[16] D. Geyer, A. Kempf, A. Dreizler, J. Janicka, Proc. Combust. Inst. 30 (2004) 681–689.

[17] J.H. Frank, K.M. Lyons, D.F. Marran, M.B. Long, S.H. Stårner, R.W. Bilger, Proc. Combust. Inst. 25 (1994) 1159–1166.

[18] J.B. Kelman, A.R. Masri, S.H. Stårner, R.W. Bilger, Proc. Combust. Inst. 25 (1994) 1141–1147.

[19] S.H. Stårner, R.W. Bilger, K.M. Lyons, J.H. Frank, M.B. Long, Combust. Flame 99 (1994) 347–354.

[20] D.F. Marran, J.H. Frank, M.B. Long, S.H. Stårner, R.W. Bilger, Opt. Lett. 20 (1994) 791–793.

[21] S.H. Stårner, R.W. Bilger, M.B. Long, J.H. Frank, D.F. Marran, Combust. Sci. Technol. 129 (1997) 141–163.

[22] J. Fielding, A.M. Schaffer, M.B. Long, Proc. Combust. Inst. 27 (1998) 1007–1014.

[23] J.H. Frank, S.A. Kaiser, M.B. Long, Proc. Combust. Inst. 29 (2002) 2687–2694.

[24] R.S. Barlow (Ed.), http://www.ca.sandia.gov/TNF/ (accessed 01/2005).

[25] S.H. Stårner, R.W. Bilger, R.W. Dibble, R.S. Barlow, Combust. Sci. Technol. 86 (1992) 223–236.

[26] R.W. Bilger, in: A.M.K.P. Taylor (Ed.), Instrumentation for Flows with Combustion, Academic Press, London, 1993, pp. 1–51.

[27] F.A. Williams, Combustion Theory, second ed., Benjamin/Cummings, Menlo Park, CA, 1985.

[28] J. Fielding, J.H. Frank, S.A. Kaiser, M.B. Long, Proc. Combust. Inst. 29 (2002) 2703–2709.

[29] D.G. Goodwin, http://www.cantera.org (accessed 10/2004).

[30] G.P. Smith, D.M. Golden, M. Frenklach, N.W. Moriarty, B. Eiteneer, M. Goldenberg, C.T. Bowman, R.K. Hanson, S. Song, W.C. Gardiner, V.V. Lissianski, Z. Qin, http://www.me.berkeley.edu/gri_mech.

[31] J.E. Rehm, P.H. Paul, Proc. Combust. Inst. 28 (2000) 1775–1782.

[32] S.A. Kaiser, J.H. Frank, M.B. Long, Appl. Opt., in press.

[33] R.W. Bilger, Combust. Sci. Technol. 13 (1976) 155–170.

[34] C.M. Vagelopoulos, J.H. Frank, Proc. Combust. Inst. 30 (2004) 241–249.

[35] P.H. Paul, H.N. Najm, Proc. Combust. Inst. 27 (1998) 43–50.